Aerodynamics of Small-Scale Propellers Undergoing Dynamic Variations of Rotational Speed

Aerodynamics of Small-Scale Propellers Undergoing Dynamic Variations of Rotational Speed

Alessandro Grava* and Jacopo Serpieri†
Politecnico di Torino, 10129 Turin, Italy
Luis Bernardos‡
ONERA, Polytechnic Institute of Paris, 92190 Meudon, France
and
Gioacchino Cafiero§
Politecnico di Torino, 10129 Turin, Italy

https://doi.org/10.2514/1.J066036

Typical mission profiles of small unmanned air vehicles (SUAVs) often involve maneuvers. SUAVs rapidly vary the rotational speed of their propellers to transition between different flight conditions. If such a transition is sufficiently rapid, the aerodynamic performance can be significantly affected, impacting stability, structural integrity, and noise generation. This study shows that dynamic rotational speed variations primarily influence the flowfield induced by the propellers. A lag effect occurs in the induced velocity owing to the fluid inertia, mainly affecting the angle of attack seen by the blades. This particularly increases during acceleration and decreases during deceleration and may lead to significant variations in thrust and torque. The main vortex structures in the wake are also affected, with rapid maneuvers potentially inducing early vortex breakdown and turbulent transition. The aerodynamic effects of dynamic rotational speed variations are investigated using a midfidelity vortex particle method solver, chosen for its low computational cost and ease of implementing such maneuvers. The code proved to be an efficient tool, supporting investigations of dynamic propeller effects for performance evaluation and the design of future SUAVs.

Nomenclature

C_T = nondimensional integral thrust coefficient, equal to $T/\rho\pi R^2(\Omega R)^2$
C_Q = nondimensional integral torque coefficient, equal to $Q/\rho\pi R^3(\Omega R)^2$
c = blade chord, m
c_D = nondimensional blade element drag coefficient
c_L = nondimensional blade element lift coefficient
f_0 = intensity of the enstrophy control filter
L^2 = relative norm of the averaged axial velocity field, %
M = Mach number
N_{cr} = critical boundary-layer disturbance integral amplification
n = revolutions per minute, rpm
$\dot{n}$ = rate of change of the rotational speed, rpm/s
Q = second invariant of the velocity gradient tensor, s^{-2}
R = propeller radius, m
Re_c = rotational chord-based Reynolds number, equal to $c\Omega r/\nu$
r = reference coordinate along the propeller radius, m
s_{C_T} = nondimensional sectional thrust along the blade span
u' = induced tangential velocity of blade elements in the rotating frame, m/s
V_z = velocity field component in the z axis, m/s
$\bar{V}_z$ = averaged velocity field component in the z axis, m/s
V_∞ = axial inflow velocity, m/s
v' = induced velocity of blade elements in the direction of the propeller's rotation axis, m/s
W = relative velocity seen by blade elements, m/s
x = axis coinciding with the radial direction at the flow investigated plane
z = axis coinciding with the axial direction at the flow investigated plane
α = angle of attack, deg
Γ_v = tip-vortex circulation, m^2/s
$\Delta(\cdot)$ = absolute difference between steady-state and dynamic cases
$\Delta\psi$ = azimuthal angle swept by the blades per time step, deg
$\delta(\cdot)$ = relative difference between steady-state and dynamic cases, %
ρ = air density, kg/m^3
Ω = propeller angular speed, rad/s
ω_y = vorticity field component in the y axis, rad/s

Received 27 June 2025; accepted for publication 19 January 2026; published online Open Access 11 March 2026.

*Ph.D. Candidate, Department of Mechanical and Aerospace Engineering, Corso Duca degli Abruzzi 24; alessandro.grava@polito.it. Member AIAA (Corresponding Author).
†Assistant Professor, Department of Mechanical and Aerospace Engineering, Corso Duca degli Abruzzi 24.
‡Aerodynamics Research Engineer, Aerodynamics, Aeroelasticity and Acoustics Department.
§Associate Professor, Department of Mechanical and Aerospace Engineering, Corso Duca degli Abruzzi 24. Member AIAA.

I. Introduction

THE popularity of small unmanned air vehicles (SUAVs) has grown significantly in recent years. Small multipropeller drones have attracted attention from both industry and investors [1] because of their distinctive characteristics, such as being lightweight, consuming little energy, and offering high maneuverability. SUAVs are often used in missions demanding long endurance and efficient operation, such as territorial monitoring [2] and agricultural spraying [3]. They have also been extensively deployed in military operations [4], with further growth anticipated in civil applications, particularly in urban environments [5]. In these latter scenarios, SUAVs must perform rapid and precise maneuvers while maintaining stability. Urban settings particularly expose aerial vehicles to numerous challenges, including obstacle avoidance and sudden wind gusts. Therefore, understanding how dynamic maneuvers influence the flowfield is crucial for providing designers and certification authorities with insights into the interaction between maneuvers and aerodynamic performance.

So far, the aerodynamic performance of SUAVs has been predominantly investigated under steady-state conditions, focusing on

the most typical operating points encountered throughout canonical missions. Among these studies, a significant body of work has concentrated on propellers in hovering (e.g., [6–9]), a condition that is both energetically demanding and complex from a fluid dynamics perspective. Concurrently, numerous investigations have investigated propellers operating in forward flight and during vertical climb. These conditions have been simulated through the interaction of the propellers with an edgewise crossflow (e.g., [10–14]) and an axial inflow (e.g., [15,16]), respectively. Although these operating conditions are well studied in classical rotorcraft aerodynamics (e.g., [17–20]), recent research on small drone propellers has revealed complex transitional flow phenomena due to the low chord-based Reynolds numbers (Re_c) characteristic of their small blades. Such phenomena substantially influence aerodynamic performance and are highly dependent on the local Reynolds number [21,22] and on the level of flow turbulence [23]. Specifically, for Re_c between 50,000 and 500,000, the laminar boundary layer separates near the leading edge, transitions to turbulence, and reattaches downstream, forming a laminar separation bubble [24]. For Re_c below 50,000, the freestream energy may be insufficient to trigger transition, resulting in massive flow separation and unsteady vortical structures [22].

Despite the extensive literature on steady-state drone aerodynamics, the investigation of dynamic maneuvers has received comparatively limited attention. Yet, understanding these maneuvers is crucial because SUAVs are routinely required to perform rapid adjustments to correct their attitude or to follow prescribed trajectories. Such maneuvers can be executed in a quasi-steady manner, smoothly transitioning between operating points, or abruptly to avoid obstacles or rapidly stabilize the vehicle under external disturbances, including gusts or sudden changes in flow conditions. Consequently, drones must be capable of rapid tilting and acceleration maneuvers, which can substantially influence propeller aerodynamic performance, affecting vehicle stability, aeroacoustic emissions, and structural integrity. Only a few studies have specifically addressed the effects of dynamic maneuvers on unmanned air vehicle (UAV) performance, and these are mostly limited to larger propellers or large vertical takeoff and landing (VTOL) aircraft. Möhren et al. [25] analyzed the impact of revolutions per minute (rpm) variations on fatigue and transient loads in VTOL propellers, demonstrating that blade deformations induced by dynamic inertial loads become significant at high acceleration rates compared to steady-state conditions. Given that dynamic rpm changes are expected to occur frequently during UAV operation, fatigue induced by such maneuvers should be considered in the design process. The same authors later examined aeroacoustic effects [26], showing that rotational speed variations and horizontal accelerations during climb and transition maneuvers contribute markedly to noise emissions. Pavel [27] investigated the influence of dynamic maneuvers, including pitch and rpm variations, on VTOL control systems and stability, demonstrating that the coordinated control of pitch and rpm can enhance stability and mitigate transient effects. Similarly, Zosimovych [28] provided a detailed methodology for modeling transient dynamics during critical VTOL operation phases, enabling the prediction of flight behavior under nonsteady conditions. Collectively, these studies highlight the importance of accounting for dynamic maneuvers in the preliminary design and control strategies of electric VTOL drones, including scenarios involving engine failure or other off-nominal operating conditions.

This study focuses on a small SUAV propeller operating in axial inflow and subjected to dynamic rpm variations imposed through a linear ramp over time. Acceleration and deceleration maneuvers in axial inflow, respectively, represent vertical climbing and descent, achieved by increasing or decreasing the rpm of the drone propellers. Unlike larger aircraft, most small-scale drones perform such maneuvers predominantly by varying the rotational speed rather than using collective or cyclic pitch adjustments. Early attempts at designing small variable-pitch propellers have been reported in the literature [29], demonstrating promising aerodynamic performance; however, their implementation on SUAVs remains challenging due to size constraints, making fixed-pitch propellers the prevailing standard. Moreover, dynamic rpm variations in axial inflow also mimic forward-flight accelerations and decelerations in fixed-wing SUAVs, in which the propellers act as thrusters with axes of rotation nearly parallel to the vehicle's direction of motion.

The objective of this study is to investigate in detail the aerodynamic effects induced by dynamic rpm variations on an isolated propeller with radius $R = 7.5$ cm, operating at chord-based Reynolds numbers Re_c ranging from 5000 to 30,000. As will be shown, the propeller-induced flowfield is strongly influenced by the dynamic rpm variations, exhibiting a lag relative to the blade motion. Consequently, the propeller interacts with an induced wake that differs from its steady-state counterpart, resulting in dynamic loads that increasingly deviate from steady-state values as the rate of change of rotational speed increases. Reproducing rotational speed variation maneuvers presents substantial challenges. Experimentally, implementing a precise rpm ramp is complicated by the coupling between the propeller and the inertia of the rotating components, as well as the limited response speed of the control system. Additionally, separating inertial from aerodynamic effects in postprocessing is difficult, leading to high uncertainties in the measurements of the aerodynamic torque. Numerically, the primary challenge is the high computational cost: whereas steady-state cases require only a few revolutions to reach convergence, dynamic maneuvers must be simulated in their entirety and repetitively, demanding substantial computational resources. High-fidelity methods, such as large-eddy simulations (LESs) or unsteady Reynolds-averaged Navier–Stokes (URANS), are generally prohibitive in this context. To overcome these limitations, this study used the midfidelity vortex particle solver VULCAINS [30,31], developed in-house at ONERA. VULCAINS uses a mesh-free vortex particle method (VPM), solving the vorticity form of the Navier–Stokes equations in a Lagrangian framework. This approach is particularly well suited for vorticity-dominated flows, accurately preserving vortical structures while avoiding the numerical dissipation associated with conventional mesh-based techniques, such as URANS or LES. It achieves satisfactory accuracy for both low-fidelity conceptual design applications [32–34] and higher-fidelity simulations [35–37], offering a significant reduction in computational cost compared to traditional high-fidelity methods. In VULCAINS, lifting surfaces (including propeller blades) are modeled using a lifting-line approach or optionally with a higher-fidelity hybrid method incorporating near-wall URANS computations [31]. In this study, the lifting-line approach was adopted to minimize computational cost, having been previously validated for the same propeller under steady-state conditions in the work of Grava et al. [38].

The remainder of this study is organized as follows. Section II provides an introduction to the main effects of dynamic rpm variation on propeller aerodynamics, summarizing the VPMs with a specific focus on VULCAINS and the simulation of maneuvers. Section III presents the comparison between steady-state and dynamic cases under different operating conditions. Finally, Sec. IV provides the conclusions, along with a brief discussion on the outlook of this study.

II. Methodology

A. Effect of Dynamic Rotational Speed Variation

The objective of this section is to illustrate the effects of a dynamic rotational speed variation maneuver on a propeller operating under axial inflow conditions. A rapid acceleration was found to increase thrust and torque with respect to the steady-state loads at the same rotational speed. Conversely, a deceleration maneuver resulted in a reduction of the aerodynamic loads.

To elucidate the physical mechanisms underlying this behavior, the velocity triangles associated with a blade element located at a radial distance r from the hub are compared between a steady-state condition and a dynamic condition at the same rotational speed n. Figure 1a shows the velocity triangle corresponding to the steady-state case. In the tangential direction, the velocity component is

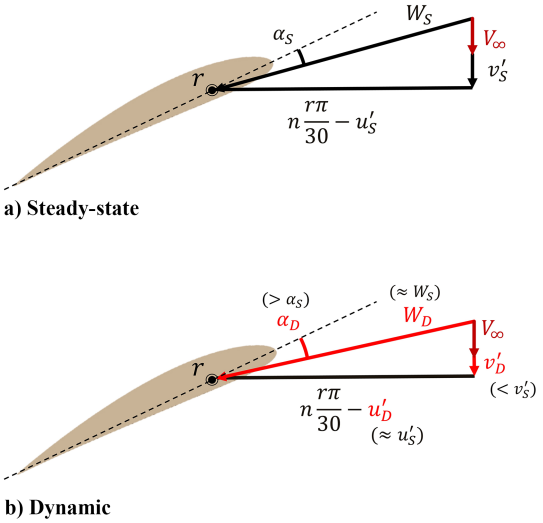

Fig. 1 Schematic representation of a blade element under a) steady-state and b) dynamic conditions.

given by $nr\pi/30 - u'_S$, where the subscript S denotes steady-state conditions. In the axial direction, the freestream velocity V_∞ is added to the axial induced velocity v'_S. The vector composition of these components yields the relative velocity W_S and its orientation with respect to the airfoil chord line, namely, the angle of attack α_S.

When the propeller dynamically reaches the same rotational speed n, accelerating from a lower rpm value, the blade element is no longer subjected to the same induced velocities as in the steady-state case. From a fluid-dynamic standpoint, the induced flowfield exhibits a lag in adapting to the instantaneous propeller rotational speed due to its intrinsic fluid inertia. When the acceleration rate is sufficiently high, these lag effects become significant and influence the integral propeller loads. As shown in Fig. 1b, the dynamic condition is characterized by a reduction in v' ($v'_D < v'_S$, where the subscript D denotes dynamic conditions), whereas the tangential induced velocity u' remains negligible in magnitude compared to the kinematic contribution associated with blade rotation. The lower v'_D primarily affects the relative velocity in terms of its orientation rather than its magnitude, resulting in an increase in the angle of attack ($\alpha_D > \alpha_S$). This increase directly leads to greater thrust and torque values on the blades at the same rotational speed. The magnitude of W is also slightly modified; however, this effect is of secondary importance compared to that associated with the change in angle of attack. A more detailed discussion of this aspect is provided in the Appendix. When the rpm variation occurs sufficiently slowly, the lag effects of the induced flowfield become negligible, and the maneuver can be regarded as quasi-steady.

The wake topology downstream of the propeller is also affected by the acceleration maneuver. As the rotational speed increases, the flowfield progressively adapts to the instantaneous operating condition, leading to a shrinking of the wake and to the concentration of the main vortical structures toward the propeller axis. This behavior reflects a dynamic transition from a high-efficiency operating condition to a lower-efficiency one as V_∞ is kept constant. For high rpm variation rates, the wake topology can change within only a few propeller revolutions, and adjacent vortices may exhibit markedly different trajectories and strengths. At low inflow velocities, this may anticipate or delay vortex interactions, thereby influencing the onset of wake turbulence. At higher inflow velocities, the vortices are more widely spaced in the axial direction, and their interaction is rarely observed in the near wake, even for high rpm variation rates.

B. Vortex Particle Method

In this section, the basic theory behind the viscous VPMs is summarized, with a focus on the VULCAINS code [39] deployed for the current investigation.

1. Problem Formulation

A viscous, unbounded, and incompressible flow can be resolved by formulating the Navier–Stokes equations into their vorticity form. This is done by taking the curl over the original momentum equation from a Lagrangian point of view, leading to the expression in Eq. (1), given $\boldsymbol{\omega} = \nabla \times \boldsymbol{U}$ as the flow vorticity:

$$\frac{D\boldsymbol{\omega}}{Dt} = \frac{\partial \boldsymbol{\omega}}{\partial t} + (\boldsymbol{U}\cdot\nabla)\boldsymbol{\omega} = (\boldsymbol{\omega}\cdot\nabla)\boldsymbol{U} + \nu\Delta\boldsymbol{\omega} \tag{1}$$

The material derivatives expressed in Eq. (1) are well suited for a Lagrangian description. The two terms on the right-hand side account for the vortex stretching and the viscous effects in the flow. The flow is spatially discretized by introducing a finite set of particles, which act as a radial-basis Gaussian function of core radius σ. Each particle induces velocity at any point of the flowfield according to the Biot–Savart law. This discretization process is equivalent to a spatial filter of size σ. Hence, all flow structures smaller than σ cannot be resolved, and they represent the unresolved scales. For the VPM to converge, the particles must overlap [40], that is, the interparticle distance h must satisfy $h < \sigma$. Equation (1) can be filtered in space to account for such unresolved scales, and therefore, a term $\boldsymbol{E}_{\text{trunc}}$ appears on the right-hand side. The term in Eq. (2) represents the error between the resolved and unresolved quantities, due to the filtering of the small scale [41]. A turbulent viscosity model can be used for its approximation because it represents the enstrophy loss transferred to the small scales. In Eq. (2), $\tilde{\boldsymbol{\omega}}$ is the filtered vorticity, and ν_t is the turbulent kinematic viscosity. The superscript t refers to the transpose operator. The second term on the right-hand side is neglected [42]:

$$\boldsymbol{E}_{\text{trunc}} = -\nabla\cdot(\nu_t[(\nabla\times\tilde{\boldsymbol{\omega}}) + (\nabla\times\tilde{\boldsymbol{\omega}})^t]) \tag{2}$$

Each particle is characterized by a strength $\boldsymbol{\alpha}_s$, obtained by integrating the vorticity of the flow in the volume of the particles. The vorticity of the flow can, in turn, be retrieved from the strength of the particles, taking into account a Gaussian distribution for the spatial filter. The evolution equation of the strength of the particles is written in Eq. (3):

$$\frac{\mathrm{d}\boldsymbol{\alpha}_{s_i}}{\mathrm{d}t} = (\boldsymbol{\alpha}_{s_i}\cdot\nabla^t)\boldsymbol{U}_i + V_i\nabla\cdot((\nu+\nu_{t_i})(\nabla\times\boldsymbol{\omega}_i)) \tag{3}$$

The flow velocity is obtained with the Helmholtz decomposition theorem as $\boldsymbol{U} = \boldsymbol{U}_\infty + \boldsymbol{u}_\phi + \boldsymbol{u}_\psi$, where the last two terms correspond to the curl-free and solenoidal parts of the total velocity, respectively. No irrotational sources are considered in this approximation; the only contributions to the total velocity are the freestream velocity and the divergence-free velocity, which is induced by the particles and is obtained from the Biot–Savart law as in Eq. (4):

$$\boldsymbol{u}_\psi = \int_V \frac{1}{4\pi r^3}\boldsymbol{\omega}\times\boldsymbol{r}\,\mathrm{d}V \tag{4}$$

The solenoidal velocity is regularized by a smoothing function, obtained directly from the spatial filter. The particles are advected in the flow according to the total velocity. In this study, the curl-free velocity sources $\boldsymbol{u}_\phi$ are neglected, thus leading to Eq. (5), which is used to compute the position of each particle $\boldsymbol{x}_i$:

$$\frac{\mathrm{d}\boldsymbol{x}_i}{\mathrm{d}t} = \tilde{\boldsymbol{U}}(\boldsymbol{x}_i, t) \approx \boldsymbol{U}_i = \boldsymbol{U}_\infty + \boldsymbol{u}_{\psi_i} \tag{5}$$

The direct solution of the terms involved in the vorticity equation is costly, being the interparticle interaction of $\mathcal{O}(N^2)$. The fast multipole method can be used to efficiently reduce these interactions and the cost to approximately $\mathcal{O}(N)$. The open-source module ExaFMM [43] was considered for the purpose, parallelized with OpenMP.

2. Viscous Treatment of the Flow

One of the principal advantages of VPM, compared to other potential flow methods, lies in its intrinsic ability to account for viscous effects. The diffusion term of the VPM equations can be solved to simulate viscous interactions among vortex structures. The VULCAINS code implements three different schemes for diffusion modeling: core spreading method, particle strength exchange, and diffusion velocity method (DVM). The DVM particularly aims to accurately compute the diffusion effects in the flow, without requiring a frequent redistribution or excessive growth of the particle size. For such reasons, the DVM was considered in this study, and its main features are hereby summarized. For a more detailed description, see [39].

The DVM rewrites the vorticity equation as an advection equation by incorporating part of the diffusion term inside the material derivatives. The unfiltered vorticity equation in Eq. (1) can be rewritten by considering a diffusion velocity $\boldsymbol{u}_d$, as done in Eq. (6):

$$\frac{\partial \boldsymbol{\omega}}{\partial t} + \nabla \cdot ((\boldsymbol{U} + \boldsymbol{u}_d) \times \boldsymbol{\omega}) = (\boldsymbol{\omega} \cdot \nabla)\boldsymbol{U} + \nabla \cdot ((\nu \nabla + \boldsymbol{u}_d) \times \boldsymbol{\omega}) \tag{6}$$

The diffusion velocity aims to represent the diffusion occurring in the rotation plane of the particles and can be written as $\boldsymbol{u}_d = -\nu \nabla \|\boldsymbol{\omega}\| / \|\boldsymbol{\omega}\|$. In this fashion, $\boldsymbol{u}_d$ becomes singular when the vorticity becomes null, which usually happens at the edge of the domain [44,45]. This is avoided using $1/\|\boldsymbol{\omega}\| \approx \|\boldsymbol{\omega}\|/(\omega_0^2 + \|\boldsymbol{\omega}\|^2)$, where ω_0 is a cutoff vorticity set to a small fraction of the highest vorticity value in the flow [46]. Different from what was done in previous studies [44,45], in VULCAINS, the diffusion velocity is directly computed instead of updating the volume of the particles, solving the strength α_s for each particle. In this fashion, the volume of the particles V has to evolve according to $\mathrm{d}V/\mathrm{d}t = \int_V \nabla \cdot \boldsymbol{u}_d \, \mathrm{d}V$.

The diffusion velocity calculated in a discrete formulation for the particles is added to the total velocity. The complete system of equations that governs the evolution of particles with the DVM is written in Eq. (7):

$$\begin{cases} \dfrac{\mathrm{d}\boldsymbol{\alpha}_{s_i}}{\mathrm{d}t} = (\boldsymbol{\alpha}_{s_i} \cdot \nabla^t)\boldsymbol{U}_i + V_i \nabla \cdot ((\nu \nabla + \boldsymbol{u}_d) \times \boldsymbol{\omega}) \\ \dfrac{\mathrm{d}\boldsymbol{x}_i}{\mathrm{d}t} = \boldsymbol{U}_\infty + \boldsymbol{u}_{\psi_i} + \boldsymbol{u}_{d_i} \\ \dfrac{\mathrm{d}V_i}{\mathrm{d}t} = V_i \nabla \cdot \boldsymbol{u}_{d_i} \end{cases} \tag{7}$$

3. Turbulent Viscosity Modeling

The turbulent viscosity used to account for the truncation error and to close the VPM equations is computed through a model to avoid solving the smallest scales [47]. For this purpose, the mixing length theory is taken into account, as it allows the approximation of the turbulent viscosity as $\nu_t \propto \Delta^2 \|\overline{\overline{S}}\|$, where $\Delta \approx \sigma$ is the flow filter width, and $\|\overline{\overline{S}}\|$ is the strain tensor [48]. Depending on the resolved scales, ν_t can be approximated with the use of the Smagorinsky constant (C_s): $\nu_t = C_s \sigma^2 \|\bar{S}\|$. Many LES turbulent viscosity models are available in the literature, but the limited number of physical quantities directly accessible in VPM restricts the number of possibilities. Three models were implemented in VULCAINS: the Smagorinsky model, the Mansour model [49], and the Vreman model [50]. These three models come from the hypothesis of homogeneous and isotropic turbulence; each model depends on the value of the constant C_s, which can either emphasize or defuse the role of turbulence in the flow.

4. Control of the Particles

To preserve the divergence-free nature of the modeled flows and to prevent numerical instabilities, it is necessary to intervene by redistributing, resizing, or reorienting the particles according to the vorticity field. In this section, an enstrophy-based control filter developed in VULCAINS is introduced. The intensity of this filter can be increased or decreased by the user through the scalar f_0. This filter results in impacting the flow solution, mostly in highly turbulent flows, as the wake of a propeller in hover or at high Reynolds numbers. Pedrizzetti [51] previously proposed a filtering approach based solely on the reorientation of particles, with only a minor side effect on their magnitude. In VULCAINS, a new approach based on the active control of the enstrophy ($\mathcal{E}$) is proposed. After each subiteration of the Runge–Kutta integration scheme, the particle strength is adjusted both in magnitude ($\|\boldsymbol{\alpha}_s\|$) and direction ($\hat{\alpha}_s$), according to $\boldsymbol{\alpha}_{s_{\text{new}}} = \boldsymbol{\mathcal{F}}_{\mathcal{E}}(\boldsymbol{\alpha}_s, \Delta t_0) = \mathcal{F}_{\text{mag}}(\boldsymbol{\alpha}_s, \Delta t_0)\boldsymbol{\mathcal{F}}_{\text{dir}}(\boldsymbol{\alpha}_s, \Delta t_0)$. The two filters of magnitude $\mathcal{F}_{\text{mag}}$ and direction $\boldsymbol{\mathcal{F}}_{\text{dir}}$ are defined as functions of the particle strength and depend on the time interval Δt_0 over which they are applied. The filters can be initially defined as in Eq. (8), where f_{mag} and f_{dir} are the cutoff frequencies of the two filters, and $\mathcal{E}$ is the enstrophy of the flow ($\mathcal{E} = \int_{R^3} \|\nabla \times \boldsymbol{U}\|^2 \, \mathrm{d}V$) in its filtered and self-induced forms ($\tilde{\mathcal{E}}_0$, $\tilde{\mathcal{E}}_{f_0}$):

$$\begin{cases} \mathcal{F}_{\text{mag}}(\boldsymbol{\alpha}_s, \Delta t_0) = 1 + \Delta t_0 f_{\text{mag}} \left(\sqrt{\dfrac{\tilde{\mathcal{E}}_0}{\tilde{\mathcal{E}}_{f_0}}} - 1 \right) \\ \boldsymbol{\mathcal{F}}_{\text{dir}}(\boldsymbol{\alpha}_s, \Delta t_0) = (1 - \Delta t_0 f_{\text{dir}})\boldsymbol{\alpha}_s + \Delta t_0 f_{\text{dir}} \dfrac{\|\boldsymbol{\alpha}_s\|}{\|\nabla \times \tilde{\boldsymbol{U}}\|} \nabla \times \tilde{\boldsymbol{U}} \end{cases} \tag{8}$$

Using constant values of f_{mag} and f_{dir} may lead to inadequate adjustments of particle properties, trying to match the local divergence-free fields. If the particle vorticity is not already close to the vorticity field in terms of magnitude and orientation, sudden and often insufficient changes might occur to their magnitude and direction features. The cutoff frequencies are hence written as a function of the particle enstrophy, calibrating their property changes with respect to this quantity. The magnitude of the cutoff frequency is tailored according to the particle strength to avoid the spatial filtering of weak particles and to overlook the strong ones ($f_{\text{mag}_i} \propto \mathcal{E}_{f_i} - \bar{\mathcal{E}}$) for each i particle, where $\bar{\mathcal{E}}$ is the mean enstrophy of the flow. The directional cutoff frequency is instead updated based on the angle between each particle's vorticity and the vorticity field. The nonconstant cutoff frequencies can be written as in Eq. (9), where f_{mag_0} and f_{dir_0} are the user-defined constants, and $\mathcal{E}_0$ is the maximum enstrophy among the particles immediately shed by the propeller blades:

$$\begin{cases} \Delta t_0 f_{\text{mag}_i} = f_{\text{mag}_0} \dfrac{\tilde{\mathcal{E}}_i - \bar{\mathcal{E}}}{\mathcal{E}_0 - \bar{\mathcal{E}}} \\ \Delta t_0 f_{\text{dir}_i} = \frac{f_{\text{dir}_0}}{\pi} \arccos \left(\dfrac{\tilde{\mathcal{E}}_i}{\|\boldsymbol{\alpha}_{s_i}\| \cdot \|\nabla \times \tilde{\boldsymbol{u}}_i\|} \right) \end{cases} \tag{9}$$

As a best practice, the authors suggest the use of $f_{\text{mag}_0} = \Delta\psi f_0$ and $f_{\text{dir}_0} = 2\Delta\psi f_0$ for the rotating lifting lines, where $\Delta\psi$ is the azimuthal angle swept per each time step. The enstrophy filter is consequently controlled by the user, varying the cutoff frequency f_0, which must be increased for highly turbulent flows, such as the wake of a propeller in hovering.

5. Coupling with Lifting Lines

The propeller blades are simulated with a lifting-line module, added to VULCAINS for its low computational cost and simplicity, following the approaches proposed in the literature [52,53]. The two lifting lines are discretized with a hyperbolic tangent distribution along the radial direction, with the smallest segments located close to the blade tips and roots. The lifting lines are moved according to the rotation axis of the propeller to simulate its motion. As the blades rotate, discrete particle sources are shed from the lifting lines with a vorticity value that preserves the local circulation calculated on the corresponding lifting-line element. The local angle of attack is computed by considering the kinematic velocity of the lifting

lines, the freestream velocity, and the induced velocity from the particle sources. The aerodynamic loads on each segment are computed using an airfoil aerodynamic database, which provides lift and drag coefficients as functions of the local angle of attack, Reynolds number, and Mach number. Once the loads are computed, it is possible to calculate the relative circulation with the Kutta–Joukowski theorem. According to Kelvin's theorem, the introduction of a solid in the flow needs to be balanced with vorticity generation due to the variations of circulation in the lifting lines. To satisfy this, particle sources are shed from the lifting lines and set free in the wake. The particles are generated with a distribution that can also be independent of the discretization of the lifting lines. In the current application, it is appropriate to shed more particles close to the blade tips to properly capture the tip vortex dynamics. The particles generated in the wake induce a velocity on the blade elements, thereby affecting the angle of attack and consequently the loads and circulation.

The lifting-line approach adopted in this study does not allow the explicit modeling of nonlifting bodies, such as the propeller hub. Although small differences are expected, previous validation studies conducted both in hovering and in axial inflow conditions [38,54] have shown that the hub has a negligible impact on the integral aerodynamic loads and on the mean flow features. It is therefore assumed that neglecting the hub only leads to local discrepancies close to the blade root and, because the kinematic velocity in this region is small, its contribution to the local and integral loads is negligible, and the effect on the mean flow features can be safely disregarded.

C. VPM Simulation Setup

The considered propeller has a radius $R = 7.5$ cm and features two blades, simulated between $r/R = 0.2$ and r/R with two rotating lifting lines positioned at a chordwise location equal to $0.25c$. The main geometric features of the blades are shown in Fig. 2, namely, chord distribution (c/R), twist angle (β), sweep angle (Λ), and dihedral angle (Γ), which are plotted as a function of the blade span. The two lifting lines are discretized with $N = 100$ elements, in which the root and tip segments have a length of $2(0.8R)/(N-1)$, whereas the length of the intermediate segments is defined through a hyperbolic tangent function between the extremes. In the region between $r/R = 0.2$ and $r/R = 1$, the blades are characterized by NACA 4412 airfoils.

The airfoil aerodynamic database was obtained using XFOIL, based on the validation results reported by Grava et al. [38]. The integral loads were found to be in close agreement with experimental data and with URANS simulations performed under flow conditions similar to those of this study. The airfoil database was calculated at a fixed Mach number of $M = 0.2$ for $Re_c = 10{,}000$, 20,000, and 30,000 and from $\alpha = -5$ deg to $\alpha = 20$ deg. The $c_L(\alpha)$ and $c_D(\alpha)$ curves were obtained by considering the boundary-layer disturbance integral amplification evaluated at the transition location (N_{cr}) equal to 5, as shown in Fig. 3. When the local angle of attack or Reynolds number lies outside the range covered by the selected airfoil database, the aerodynamic coefficients are extrapolated by

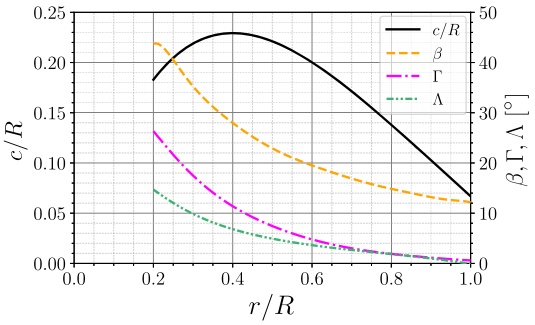

Fig. 2 Geometrical features of blades along the blade span direction: chord distribution (c/R), twist angle (β), sweep angle (Λ), and dihedral angle (Γ).

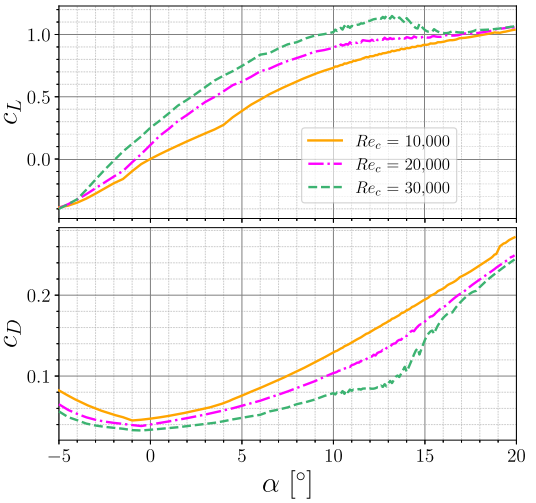

Fig. 3 Lift ($c_L(\alpha)$) and drag ($c_D(\alpha)$) coefficients of the NACA 4412 airfoil computed using XFOIL.

blending the available database with a reference dataset corresponding to the NACA 0012 airfoil under post-stall conditions [55].

The main parameters of VPM computation were chosen as a consequence of the parametric analysis performed in [38]. In particular, the number of particle sources shed by each blade at each iteration was set to 50, and the azimuthal angle swept per iteration $\Delta\psi$ was set to 5 deg. Furthermore, a third integration order was chosen for the Runge–Kutta scheme, whereas the DVM and Vreman model were chosen as the diffusion scheme and turbulent viscosity model, respectively. Finally, a value of 0.75 was set to regulate the intensity of the enstrophy control filter f_0. These parameters ensured a good balance between accuracy and computational cost in [38].

1. *Implementation of Rotational Speed Variations in VPM and Simulation Matrix*

The dynamic variation of rotational speed is performed by updating the value of n at each iteration i, based on the type and rapidity of the maneuver. In this study, a simple ramp was considered, corresponding to a linear function of n over time. Thus, n was updated at each time t_i to n_i, as in Eq. (10):

$$n_i = n_{\text{Start}} + \frac{n_{\text{End}} - n_{\text{Start}}}{t_r} \cdot (t_i - t_{\text{Start}}) \tag{10}$$

The subscript Start refers to the start of the maneuver; in the current simulation matrix, n_{Start} was set to 3000 rpm for acceleration and 7000 rpm for deceleration. The value of t_{Start} was chosen to perform around 80 revolutions to reach a converged steady state before the start of the maneuver, corresponding to 1.5 s for acceleration and 1 s for deceleration maneuvers. The rpm value reached at the end of the maneuvers, denoted by n_{End}, was set to 7000 rpm for acceleration and 3000 rpm for deceleration. Finally, t_r refers to the time needed to perform the maneuvers. To maintain a constant $\Delta\psi$ equal to 5 deg throughout the simulations, it was necessary to update the value of the time step Δt at each iteration according to $\Delta t = \Delta\psi/(6n)$. In this way, particles are homogeneously shed throughout the propeller's revolution, even if the propeller changes its rotational speed.

The simulations were initially performed with a fixed value of $V_\infty = 3$ m/s. Three values of t_r were taken into account for the acceleration and deceleration maneuvers, leading to a comparison among three different rates of change of rotational speed ($\dot{n}$), defined as $\dot{n} = (n_{\text{End}} - n_{\text{Start}})/t_r$. The rates considered in this study were 4000, 40,000, and 80,000 rpm/s.

The results were then compared with steady-state cases, simulated between 3000 and 7000 rpm with increments of 500 rpm, in terms of the aerodynamic performance and instantaneous velocity

and vorticity fields. The vorticity field was used in conjunction with the Q-criterion [56] field to investigate the wake topology, particularly characterizing the evolution of the tip vortices.

The acceleration maneuver with $\dot{n} = 80{,}000$ rpm/s was repeated 100 times to obtain the averaged velocity field at midmaneuver (i.e., at 5000 rpm). These 100 repetitions were performed with a random initial azimuthal angle to prevent phase locking. The averaged velocity field was then compared with the time-averaged velocity fields evaluated in steady-state conditions at 3000 and 5000 rpm. To assess the convergence of the mean flowfield in the dynamic case, the relative L^2 norm was evaluated. The norm was calculated every 10 repetitions, as in Eq. (11), where $\bar{V}_{z_i}$ is the mean velocity field evaluated after i repetitions, and $\bar{V}_{z_{100}}$ is the mean velocity field evaluated after 100 repetitions:

$$L_i^2 = \frac{\|\overline{V}_{z_i} - \overline{V}_{z_{100}}\|_2}{\|\overline{V}_{z_{100}}\|_2} \tag{11}$$

The effect of the axial inflow on the flowfield stemming from the dynamic maneuver was investigated, repeating the simulation at $n = 80{,}000$ rpm/s for $V_\infty = 1.5$ m/s and $V_\infty = 4.5$ m/s.

III. Results

A. Aerodynamic Performance

In this section, the results obtained from the VPM simulations are presented. The primary goal is to analyze the main effects of linear rpm ramps at a fixed axial inflow velocity of $V_\infty = 3$ m/s. To this end, focus was initially directed to the integral load quantities, with an investigation into the causes behind the differences between dynamic and steady-state cases. The nondimensional thrust (C_T) and torque (C_Q) coefficients are shown as a function of n in Fig. 4. The acceleration and deceleration maneuvers are represented by solid and dashed lines, respectively, whereas different colors highlight the different $\dot{n}$ values. The integral values obtained under steady-state conditions are superimposed on the dynamic cases for a quantitative comparison.

Both acceleration and deceleration maneuvers were initiated from a converged steady-state operating condition; therefore, the initial thrust and torque values coincided with those obtained in the corresponding steady-state cases. As $\dot{n}$ was increased, C_T and C_Q progressively deviated from the steady-state values. During acceleration, both thrust and torque increased with increasing $\dot{n}$, whereas the opposite trend was observed during deceleration. The maneuver characterized by $\dot{n} = 4000$ rpm/s yielded results that were nearly superimposed on the steady-state cases, with relative differences in δC_T and δC_Q remaining below 1%. For the intermediate ramp, $\dot{n} = 40{,}000$ rpm/s, more pronounced deviations were observed, with maximum relative differences of approximately 4% at 4000 rpm during acceleration and about 5% at 3000 rpm during deceleration. Finally, the fastest maneuver at $\dot{n} = 80{,}000$ rpm/s exhibited maximum relative deviations on the order of 10% for both acceleration and deceleration.

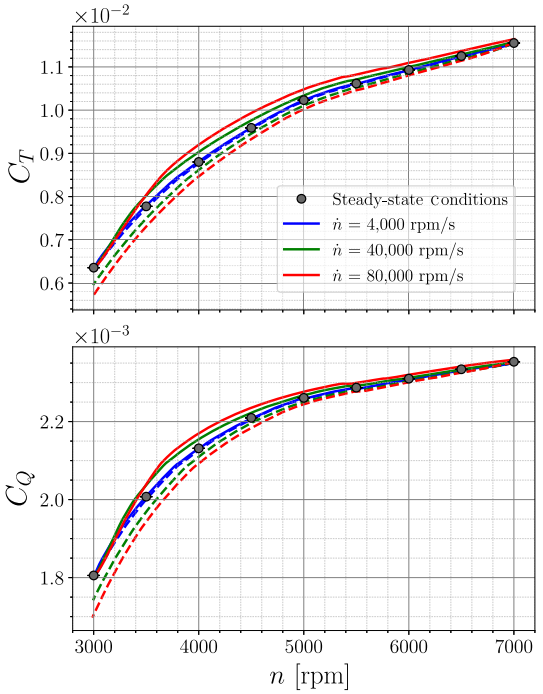

Fig. 4 C_T and C_Q as a function of n in steady-state and dynamic conditions; solid lines correspond to accelerations, whereas dashed lines indicate decelerations.

The integral load deviations observed during acceleration and deceleration maneuvers are not symmetric with respect to the corresponding steady-state values. This behavior is primarily related to the way the dynamic simulations are performed. In particular, each maneuver was initiated from a steady-state condition at the starting rotational speed, n_{Start}, such that the initial thrust and torque values initially coincided with the steady-state loads. The relative impact of the dynamic rpm variation then depends on the ratio between $\dot{n}$ and the instantaneous rotational speed n; as a consequence, the dynamic effects are more pronounced at lower rotational speeds, where $\dot{n}$ is constant. During acceleration, for instance, the maneuver started at $n_{\text{Start}} = 3000$ rpm, in which the dynamic and steady-state loads initially coincided. Shortly after the beginning of the maneuver, a significant deviation from the steady-state condition was observed, with the maximum relative differences occurring at low rpm, at $n \approx 4000$ rpm. As n was progressively increased, the relative deviation between the loads decreased, and the dynamic thrust and torque curves gradually approached the corresponding steady-state values. In contrast, during deceleration, the maneuver started at $n_{\text{Start}} = 7000$ rpm, and the ratio between $\dot{n}$ and n is the smallest in the simulation matrix. As a result, the initial deviations between dynamic and steady-state loads were limited. As the maneuver proceeded and n decreased, the relative importance of dynamic effects increased, leading to progressively larger deviations from the steady-state conditions, which reached their maximum at the end of the maneuver, at $n_{\text{End}} = 3000$ rpm.

These results indicate that, under a constant $\dot{n}$ ramp, acceleration maneuvers tend to converge toward a quasi-steady behavior at high rpm, whereas deceleration maneuvers amplify unsteady effects as the rotational speed decreases. This highlights the inherent asymmetry between acceleration and deceleration under constant $\dot{n}$ conditions. This suggests that a linear rpm ramp may not represent an optimal strategy for performing rpm variation maneuvers from the perspective of aerodynamic load control.

To investigate in detail the reasons behind the observed trends in the integral quantities, the focus is now shifted to the distribution of thrust per unit length along the blade span. This quantity is analyzed only at midmaneuver (i.e., at $n = 5000$ rpm) for both acceleration and deceleration because qualitatively similar conclusions can be drawn at different n values. The nondimensional thrust per unit length (s_{C_T}) along the blade span is first presented in Fig. 5. The s_{C_T} distribution shows the same trend observed for the integral thrust, deviating from the values of the steady-state case as $\dot{n}$ increased. The most significant differences for both acceleration and deceleration are observable between $r/R = 0.5$ and $r/R = 0.9$.

As explored in detail in the Appendix, the thrust generated by each element of the lifting line can be approximated as the lift of that element, which depends on parameters such as the square of the magnitude of the relative velocity (W^2) and the angle of attack (α). Hence, the variation in thrust and torque compared to the steady-state case is mostly attributable to the variation in these two quantities. The radial distributions of relative differences δW^2 and $\delta\alpha$ compared to the steady-state case, also extracted at 5000 rpm, are shown in Fig. 6. The relative differences observed in W^2 are generally small, even for the fastest maneuver. In particular, for $r/R > 0.4$, where the blade provided the largest contribution to the overall thrust, δW^2 remained below 1%. Larger relative variations

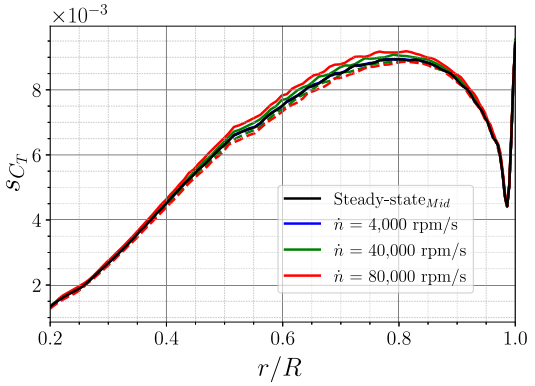

Fig. 5 Thrust per unit length s_{C_T} as a function of r/R extracted at midmaneuver; solid lines correspond to accelerations, whereas dashed lines indicate decelerations.

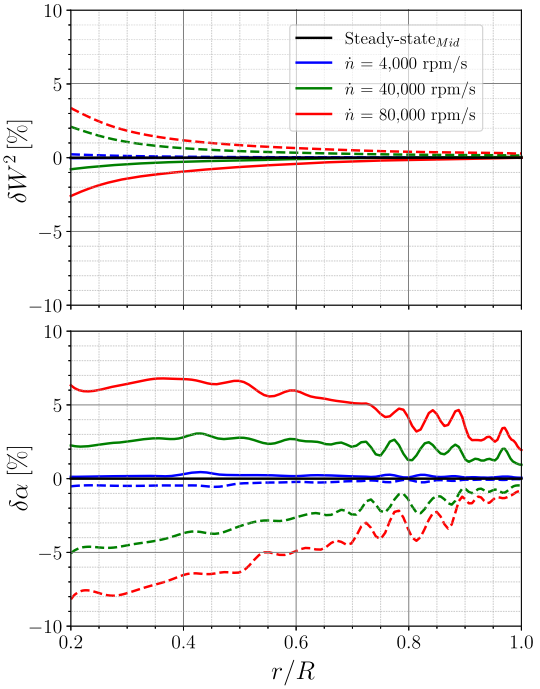

Fig. 6 Relative differences δW^2 and $\delta\alpha$ as a function of r/R extracted at midmaneuver; solid lines correspond to accelerations, whereas dashed lines indicate decelerations.

were observed in the root region, for $r/R < 0.4$, where δW^2 reached a maximum value of approximately 2.8% at $r/R = 0.2$. However, in this region, the contribution to the integral thrust and torque is negligible due to the small absolute values of W. The dominant contribution to the load variations observed in Fig. 4 is instead represented by $\delta\alpha$, which exhibited greater deviations along the blade span. Although the largest values of $\delta\alpha$ were again observed close to the hub, substantial deviations were also present in the most load-bearing portion of the blade ($r/R > 0.6$). Moreover, $\delta\alpha$ increases with increasing $\dot{n}$ during acceleration and decreases during deceleration, consistent with the trends observed in the loads. The absence of the hub may have influenced $\delta\alpha$ in the root region; however, because of the very small values of W in this blade portion, the effect on the local thrust coefficient is negligible. Consequently, the hub contribution can be disregarded when focusing on both local and integral thrust.

The effects of W^2 and α variation are found to act in opposition during dynamic maneuvers. Notwithstanding this, variations in W^2 are either negligible or overcome by the dominant effect associated with variations in α. This hierarchy between the two terms is further examined in the Appendix. It should be noted that the deviations observed in both W^2 and α remain asymmetric between acceleration and deceleration, although these quantities are extracted at the same rotational speed for the two cases. This asymmetry is indeed related to the differing histories of the two maneuvers and is consistent with the asymmetry in the integral loads previously observed in Fig. 4.

As previously anticipated in Sec. II.A, the differences between steady-state and dynamic cases can be attributed to the lag effect in the induced velocity in the wake. The velocity can be decomposed into a tangential component (u') and an axial (v') component. Thus, the variation in u' and v' is responsible for the variation in α and W^2, consequently affecting the overall performance of the propeller. The distributions of $|u'|$ and $|v'|$ along the blade span were extracted at midmaneuver ($n = 5000$ rpm) and are shown in Fig. 7, comparing the dynamic cases in acceleration and deceleration with the steady-state case. Both quantities are normalized with respect to ΩR, where Ω is calculated as $\Omega = n\pi/30$, considering $n = 5000$ rpm. The two induced velocities exhibit significant relative deviations from their steady-state values. In particular, $|u'|$ increases during acceleration and decreases during deceleration, whereas $|v'|$ follows the opposite trend. The tangential induced velocity u' is usually slightly underestimated in VPM models based on a lifting-line formulation because the vorticity shed by the boundary layer is not modeled. Because particles are released from the blade trailing edges in the tangential direction, they cannot induce velocity along the same axis. As a result, the contribution of early-age particles to u' is reduced due to their relative position within the computational domain. Nevertheless, u' is nearly one order of magnitude smaller than v' and up to two orders of magnitude smaller than Ωr, which explains why it is often neglected in preliminary or approximate analyses [17]. Consequently, even when the relative variations of the induced velocities are comparable, the influence of v' dominates, whereas the effect of u' remains negligible. A decrease in the absolute value of v' during acceleration and an increase during deceleration result in an increase and a decrease in α, respectively. Conversely, W^2 follows the opposite trend, decreasing as v' decreases and increasing as v' increases.

B. Induced Wake Instantaneous Flow Features

In this section, the main features of the flowfields in dynamic conditions are assessed through a comparison with steady-state

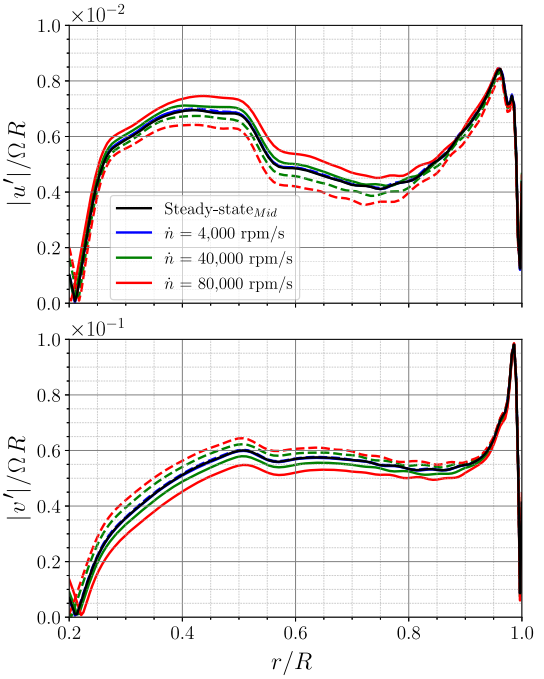

Fig. 7 Induced velocities $|u'|$ and $|v'|$ as a function of r/R extracted at midmaneuver; solid lines correspond to accelerations, whereas dashed lines indicate decelerations.

flowfields. The fields are extracted on an $x-z$ plane, where x denotes the axis oriented along the propeller radial direction, and z denotes the axis aligned with the propeller rotation axis. The flowfields are first presented in terms of instantaneous axial velocity along the z direction (V_z), extracted at midmaneuver for $n = 5000$ rpm. The dynamic maneuvers are performed to feature the same propeller azimuthal angle ψ at midmaneuver; therefore, the corresponding flowfields depict the blades aligned along the x axis. For comparison purposes, the steady-state flowfield at $n = 5000$ rpm is also reported and referred to as the steady-state$_{\text{Mid}}$ case. In addition, steady-state flowfields at $n = 3000$ rpm for acceleration and at $n = 7000$ rpm for deceleration are included and referred to as the steady-state$_{\text{Mid}}$ cases. This approach enables a direct comparison between the flow features observed during the dynamic maneuvers and those characterizing the conditions preceding the onset of the maneuvers.

The instantaneous axial velocity fields are shown in Fig. 8 in nondimensional form. For consistency, the normalization quantity ΩR was computed using $n = 5000$ rpm for all cases, including the steady-state$_{\text{Start}}$ conditions. The propeller-shaped mask was added to improve clarity. For small values of $\dot{n}$, the velocity field closely resembles the steady-state case at $n = 5000$ rpm, both in terms of axial velocity values and wake radial extent. The dynamic case characterized by $\dot{n} = 4000$ rpm/s exhibits V_z values that are very close to those of the steady-state$_{\text{Mid}}$ case, with a slight underestimation during acceleration and a slight overestimation during deceleration. As $\dot{n}$ increased, pronounced differences became evident in the wake region. In particular, during acceleration, a reduction in V_z was observed, whereas an increase occurred during deceleration, with values progressively approaching those of the steady-state$_{\text{Start}}$ case, especially at larger z/R.

Focusing on the acceleration maneuver, the wake exhibited a radial expansion as $\dot{n}$ increased. At $n_{\text{Start}} = 3000$ rpm, the propeller operated in a higher-efficiency regime, characterized by a radially wider and more cylindrical flow tube. Throughout the acceleration, the wake at larger z/R showed features similar to those observed at n_{Start}, both in terms of V_z values and radial extent. The axial velocity varied significantly along the z direction, resulting in a pronounced axial velocity gradient that became steeper as $\dot{n}$ increased.

Similar considerations apply to the deceleration maneuver. In this case, the steady-state$_{\text{Start}}$ field is characterized by higher axial velocities and a reduced radial extent as the propeller operates at lower efficiency with $n_{\text{Start}} = 7000$ rpm. For the deceleration maneuver with $\dot{n} = 80{,}000$ rpm/s, the propeller requires approximately 2.5 revolutions to decelerate from $n_{\text{Start}} = 7000$ to 5000 rpm. As the propeller is two-bladed, five pairs of symmetric tip vortices are generated within this interval in the investigated plane, identifiable as pseudocircular regions of high axial velocity in the wake, adjacent to regions of negative velocity immediately outside the wake. Beyond the fifth vortex pair, located at approximately $z/R = 1.6$, the flowfield structure closely resembles that present before the onset of the maneuver. Although this portion of the wake is generated under steady-state conditions, it remains influenced by the deceleration process, with locally reduced wake velocities at the same z/R compared to the corresponding steady-state case.

The different cases are now compared in terms of the instantaneous vorticity component along the y axis (ω_y), normalized with Ω. The vorticity color maps are shown in Fig. 9 with a similar arrangement to that of Fig. 8, allowing comparison of the dynamic cases with the steady-state cases at the start of the maneuver and at midmaneuver. The color maps feature a red (blue) color for regions of $\omega_y > 0$ ($\omega_y < 0$). A blanking is applied to the color map for values of ω_y near zero. All the displayed cases feature two main pairs of vortical structures that evolve in the axial direction and are symmetric with respect to the z axis. The first and strongest pair of structures is composed of the tip vortices, with positive vorticity at $x > 0$ and negative at $x < 0$, according to the propeller's rotation direction. The root vortices, on the other hand, are characterized by lower ω_y values than the tip vortices shed from the same blades and an opposite rotation direction. At $\dot{n} = 4000$ rpm/s, the vortex structures are similar in terms of vorticity values and position to the steady-state$_{\text{Mid}}$ cases in both acceleration and deceleration. By increasing $\dot{n}$, the structures located at high z/R values show lower ω_y values, and the wake structure resembles more the steady-state case at the start of the maneuvers.

The ω_y fields are used in conjunction with the Q-criterion fields to quantitatively characterize the evolution of the tip vortices. The Q-criterion fields in the plane x–z, normalized with respect to Ω^2, are shown in Fig. 10. The color maps are restricted to positive values only, allowing for a straightforward identification of the regions of the flowfield where the rotation prevails over the shear [57]. The Q-criterion fields allow the identification of strong tip vortices, characterized by high values of Q, as well as weaker root vortices, associated with Q values close to zero. To isolate the tip vortices and quantify their area in the x–z plane, an arbitrary threshold was applied to the normalized quantity Q/Ω^2, set to 0.8. This value represents the minimum threshold for which no root vortex is detected in the analyzed fields. Connected regions in the Q fields satisfying $Q/\Omega^2 > 0.8$ are therefore identified as tip vortices, and their center is defined in correspondence with the local maximum of Q. The area of each vortex is defined as the region surrounding this maximum where the condition $Q/\Omega^2 > 0.8$ is satisfied. Then, ω_y is

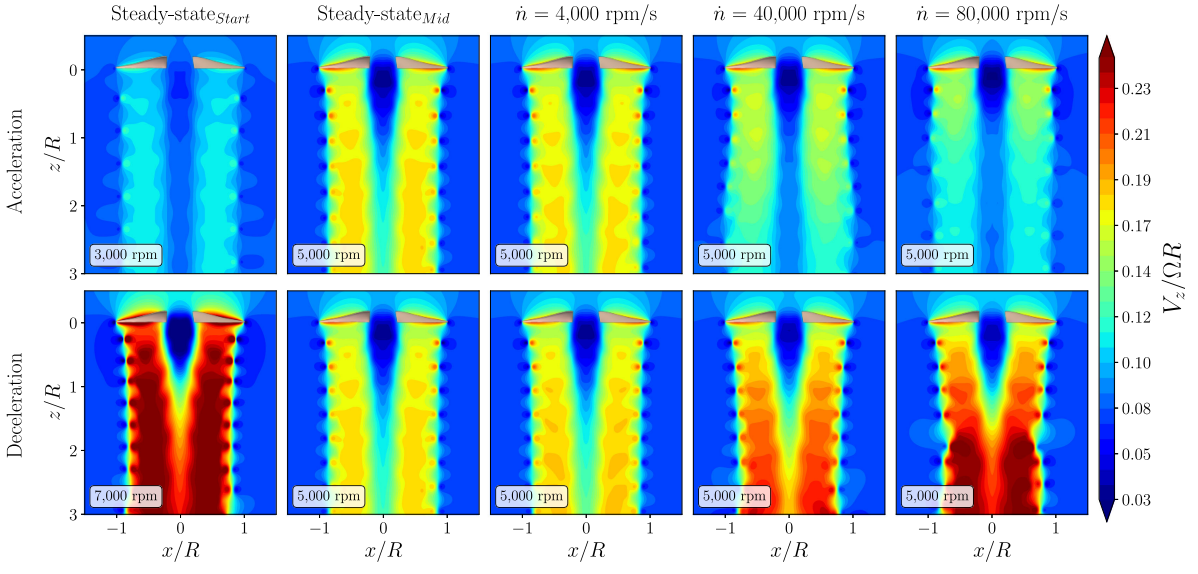

Fig. 8 Color maps of the normalized instantaneous axial velocity $V_z/\Omega R$ for the dynamic and steady-state cases.

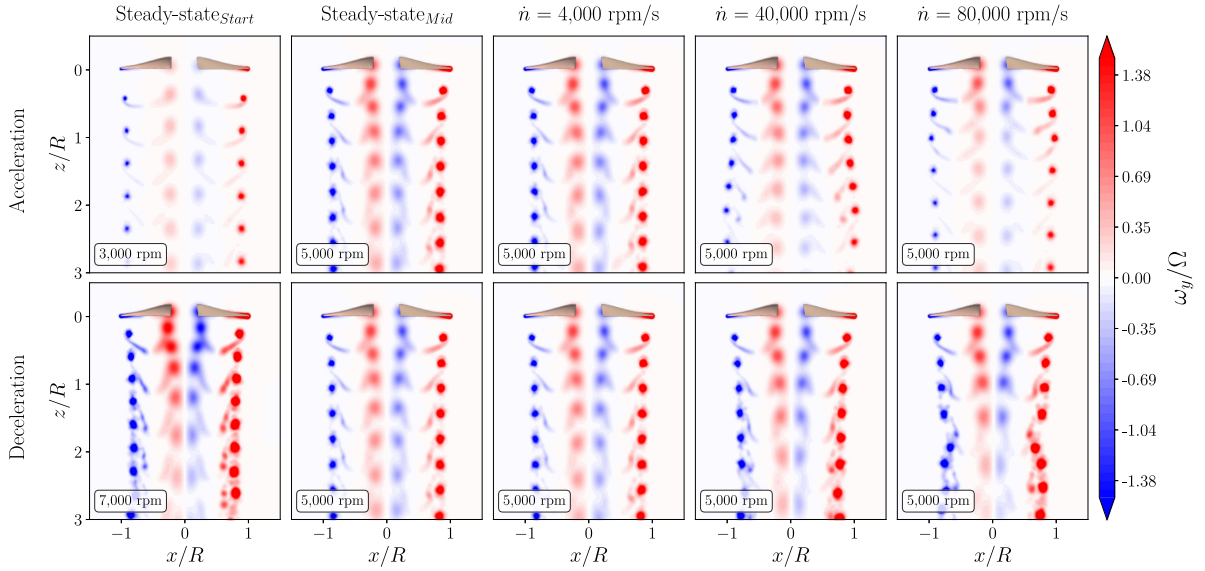

Fig. 9 Color maps of the normalized out-of-plane vorticity ω_y/Ω for the dynamic and steady-state cases.

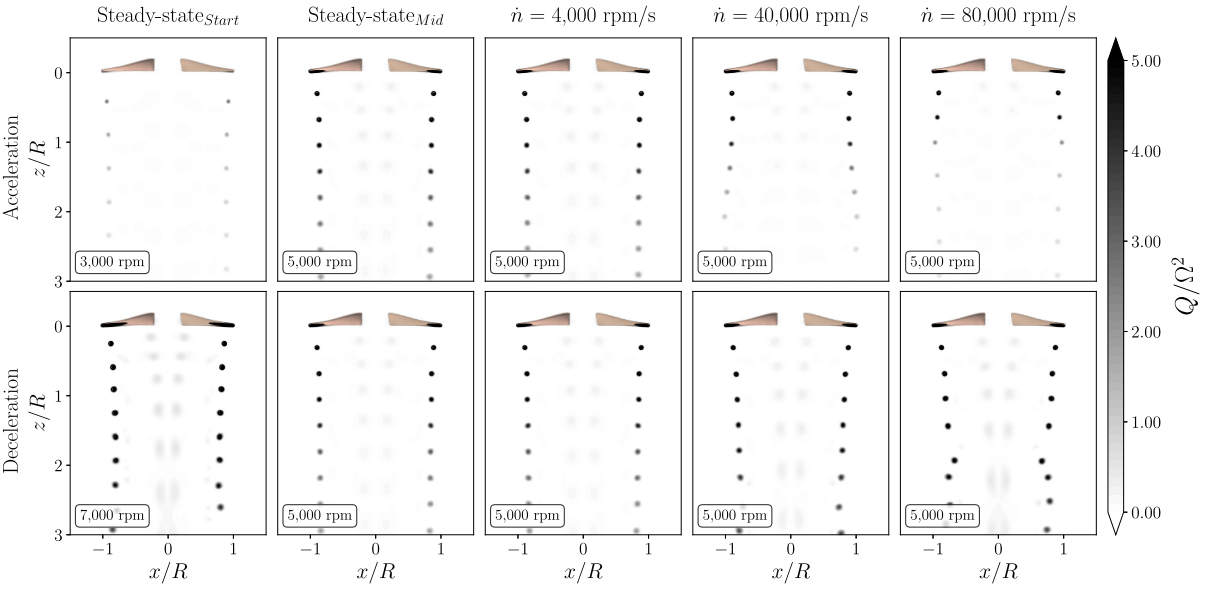

Fig. 10 Color maps of the normalized Q/Ω^2 for the dynamic and steady-state cases.

integrated over the vortex area according to the Stokes's theorem to evaluate its circulation. The choice of a different threshold to identify the tip vortex is arbitrary and may affect the evaluated circulation. However, in the light of a comparative assessment between the investigated cases, it is deemed sufficient to select the same threshold for all cases [58,59].

The comparison between the dynamic and steady-state cases in acceleration and deceleration is shown in Fig. 11 in terms of the trajectory and circulation Γ_v of the vortices. The analysis of these structures is useful for assessing the wake evolution in terms of axial and radial stretching. Because of the axial symmetry of the wake, the vortices generated by the blade positioned at $x/R > 0$ are exclusively shown. In the steady-state$_{\text{Mid}}$ case, the tip vortices were initially identified at $x/R = 0.98$ and were subsequently convected inboard, stabilizing around x/R for $z/R > 0.7$. The first identified vortex exhibited a significantly higher circulation Γ_v than the vortices located farther downstream. From the second vortex onward, the circulation decreased almost linearly with z/R, approaching zero for the last identified vortex at $z/R = 2.55$. Beyond this axial location, the Q value was insufficient to exceed the selected threshold as the vortices became progressively weaker and eventually broke down due to the reduced convective velocity of the wake and the shear induced by entrainment of the external flow.

Focusing on the acceleration results, fewer vortices were identified within the wake compared to the steady-state$_{\text{Mid}}$ case. Moreover, as $\dot{n}$ increased, the vortices were found at progressively greater radial positions, indicating a radial widening of the wake relative to the steady-state case. At the same time, the vortex circulation was reduced and tended toward zero at smaller axial distances. The upstream shift of the vortex decay with increasing $\dot{n}$ indicates that the wake is contracted in the axial direction.

In contrast, the deceleration maneuvers exhibited the opposite behavior. As $\dot{n}$ increased, the tip vortices were displaced toward lower radial coordinates, indicating a radial contraction of the wake. At the same time, the circulation increased with $\dot{n}$. Notably, for $\dot{n} = 80{,}000$ rpm/s, the circulation closely matched that of the steady-state$_{\text{Start}}$ case for $z/R > 2$. At this value of $\dot{n}$, approximately 2.5 revolutions were required to decelerate from $n_{\text{Start}} = 7000$ to 5000 rpm, resulting in the shedding of five tip vortices in the investigated plane. The sixth identified vortex, located at $z/R = 2$, was shed before the onset of the maneuver, when the propeller was still operating at 7000 rpm, and therefore exhibited a circulation

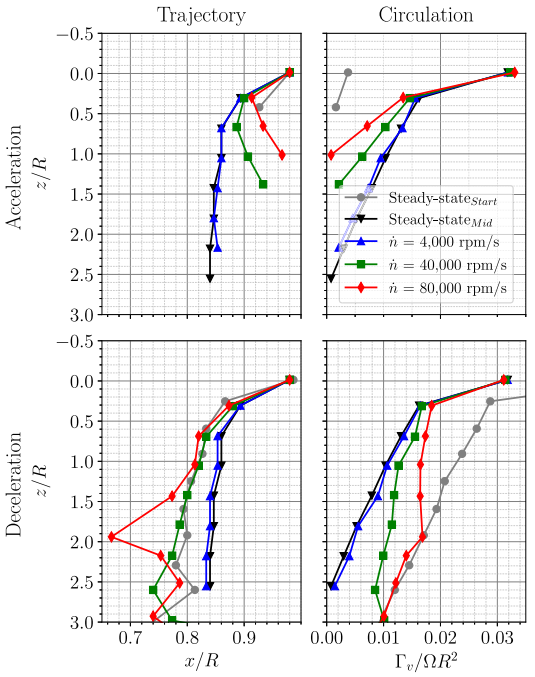

Fig. 11 Tip vortex trajectory and circulation for the steady-state and dynamic cases.

comparable to that of the corresponding vortex in the steady-state$_{\text{Start}}$ case. Finally, an additional feature was observed for the same dynamic case. An isolated vortex located at z/R underwent a sudden inboard displacement toward lower x/R, deviating from the trajectory followed by the other vortices. This behavior is likely associated with the transition from the steady-state operating condition to the onset of the dynamic maneuver. The initiation of deceleration induced an abrupt modification of the flowfield, altering both the radial and axial structures of the wake. As a result, the first vortex shed during the maneuver was convected more outboard than the one generated immediately beforehand, and their mutual interaction led to this localized deviation. Such interactions may promote vortex breakdown and an anticipated transition to a turbulent wake, particularly at high rotational speeds, in which vortex structures are stronger and more closely spaced.

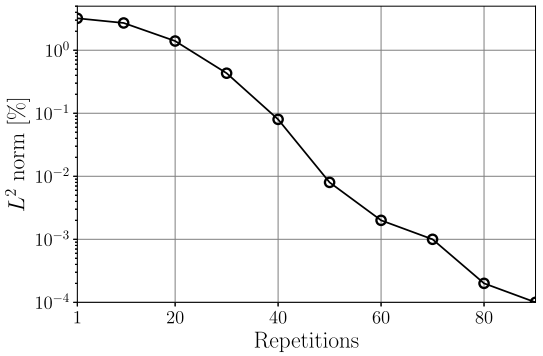

Fig. 12 Relative L^2 norm as a function of the repetitions used for the velocity field averaging in dynamic conditions.

C. Time-Averaged Flow Topology

In this section, the main differences in the averaged velocity fields between the steady-state cases and the dynamic acceleration case with $\dot{n} = 80{,}000$ rpm/s are explored in detail. To assess the convergence of the averaged dynamic velocity field at midmaneuver, the relative L^2 norm is evaluated according to Eq. (11). This quantity is shown as a function of the simulation repetitions used for the averaging of the velocity field in Fig. 12. The relative L^2 norm dropped below 1% after 30 repetitions, exhibiting an approximately exponential decay, as indicated by the linear trend on the semilogarithmic plot. Further increasing the number of repetitions continued this decay, leading to an effectively converged velocity field, with the relative L^2 norm reaching 0.02% after 50 repetitions. Beyond this point, additional repetitions did not significantly affect the averaged flowfield.

The velocity field averaged over 100 simulation repetitions was compared with the time-averaged steady-state velocity fields at 3000 rpm (steady-state$_{\text{Start}}$) and 5000 rpm (steady-state$_{\text{Mid}}$), obtained by averaging over the last 10 revolutions. The mean axial velocity ($\bar{V}_z$) fields are shown in Fig. 13, along with the axial velocity profiles extracted at $z/R = -0.25$, 1, and 2. For consistency, the normalization quantity ΩR was computed using $n = 5000$ rpm for all flowfields. The averaged velocity field under dynamic conditions exhibited features already observed in the instantaneous flowfields. In particular, a strong velocity gradient along the z direction was observed due to the temporal evolution of the wake. Close to the propeller, the velocity field resembled the steady-state$_{\text{Mid}}$ case, as indicated by the velocity profiles. At $z/R = -0.25$, the dynamic velocity values nearly overlapped with those of the steady-state$_{\text{Mid}}$ case, whereas the steady-state$_{\text{Start}}$ case exhibited significantly lower axial velocities. Moving toward larger z/R coordinates, the axial velocity in the dynamic case decreased relative to the steady-state$_{\text{Mid}}$ case, approaching the values observed at the start of the maneuver. By $z/R = 1$, the wake in the dynamic case was already wider in the radial direction than in both steady-state cases. At $z/R = 2$, the axial velocity profiles of the dynamic case and the steady-state$_{\text{Start}}$ case were almost entirely superimposed.

D. Influence of the Axial Inflow on the Propeller Performance

In this section, the influence of the axial inflow velocity V_∞ on the acceleration maneuver is assessed. Specifically, the steady-state cases and the acceleration maneuver at the highest $\dot{n}$ value ($\dot{n} = 80{,}000$ rpm/s) were repeated for two additional inflow velocities, $V_\infty = 1.5$ and 4.5 m/s. The differences observed between the

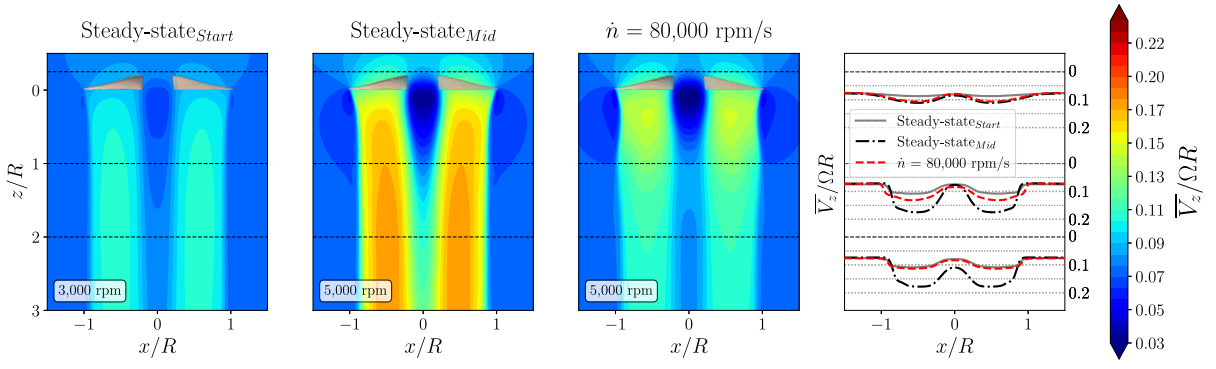

Fig. 13 Color maps of $\bar{V}_z/\Omega R$ along with velocity profiles extracted at $z/R = -0.25$, 1, and 2 (indicated by black dashed lines).

steady-state and dynamic cases are qualitatively similar to those described in the previous sections for $V_\infty = 3$ m/s. In particular, an increase in thrust and torque compared to the steady-state cases was observed, with the discrepancy between the two operating conditions being more pronounced at lower rpm. Although the trends are qualitatively similar, it is useful to examine the absolute differences between the steady-state and dynamic integral loads to assess the effect of the inflow velocity V_∞. ΔC_T and ΔC_Q are presented in Fig. 14 as a function of n, being evaluated every 500 rpm between 3000 and 7000 rpm. Both ΔC_T and ΔC_Q increased at nearly all considered n values as V_∞ was increased. This trend is largely attributable to the low Re_c regime in which the propeller operates in this study. In particular, the $c_L(\alpha)$ curves exhibit a nearly quadratic shape even at low angles of attack, whereas at higher Re_c the relationship between the two quantities is typically linear [60]. Increasing V_∞ reduces the angle of attack α experienced by the blades, such that the same difference in angle of attack between steady-state and dynamic conditions $\Delta\alpha$ leads to larger Δc_L.

The distribution of α at midmaneuver ($n = 5000$ rpm) as a function of r/R for different V_∞ values is shown in Fig. 15. Both steady-state and dynamic curves shift downward as V_∞ increases. Nevertheless, $\Delta\alpha$ between the steady-state and dynamic cases remains nearly constant in the most load-bearing portion of the blades (r/R), as illustrated in Fig. 16. Since $\Delta\alpha$ is essentially unchanged across different V_∞ values, larger Δc_L values are obtained at higher inflow velocities, thereby explaining the increase in ΔC_T and ΔC_Q with V_∞ observed in Fig. 14.

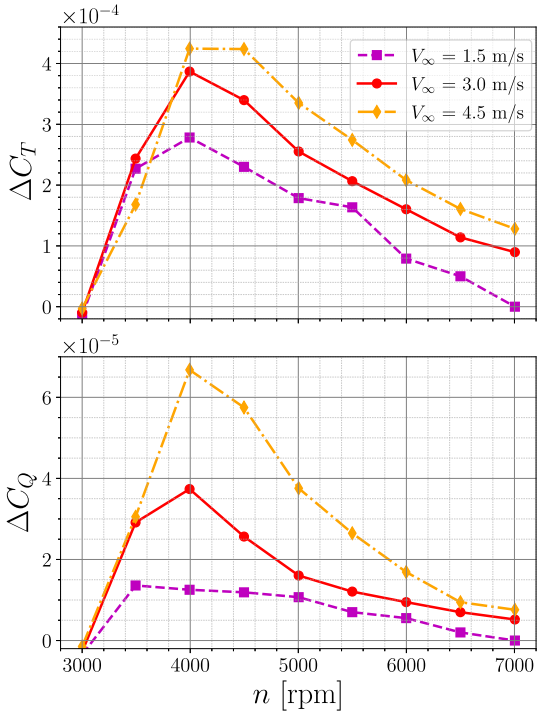

Fig. 14 ΔC_T and ΔC_Q differences between steady-state and dynamic cases with $\dot{n} = 80{,}000$ rpm/s for different V_∞ values.

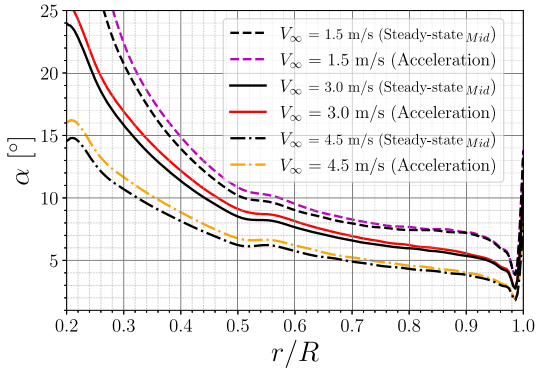

Fig. 15 Angle of attack α distribution as a function of r/R extracted at midmaneuver for different V_∞ values.

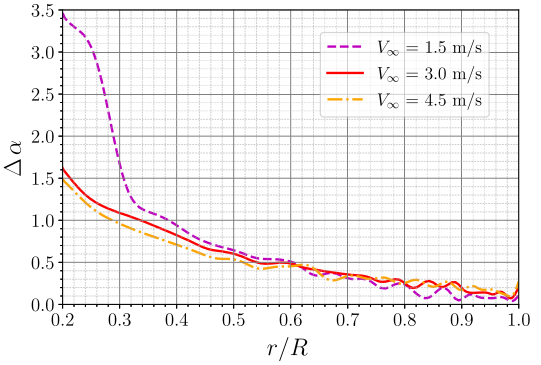

Fig. 16 $\Delta\alpha$ as a function of r/R extracted at midmaneuver for different V_∞ values.

As anticipated, the pseudoquadratic shape of the $c_L(\alpha)$ curves is characteristic of most conventional airfoils at low Reynolds numbers [60]. Therefore, the observed trends are not directly generalizable to larger propellers, featured by greater Re_c. What instead remains evident and largely independent of Reynolds number is the increase in thrust and torque during acceleration, with the opposite trend during deceleration. This effect is significant across different axial inflow velocities and thus persists both near and far from peak efficiency conditions.

IV. Conclusions

This study investigated the influence of dynamic rotational speed variations on the aerodynamics of a small-scale drone propeller operating in axial inflow. Acceleration and deceleration maneuvers were performed at different rates of change in rotational speed, with rpm linearly increasing or decreasing over time.

Key findings indicate that high rates of change lead to significant deviations in the integral thrust and torque from their corresponding steady-state values. At a given rate, this effect is more pronounced at lower rpm. The observed increase in thrust and torque during acceleration and the corresponding decrease during deceleration are primarily attributed to a lag in the induced flowfield. Under dynamic conditions, the axial component of the induced velocity is particularly affected, altering the relative velocity experienced by the blades mainly in terms of orientation rather than magnitude and consequently affecting the aerodynamic loads. This lag effect is evident in both instantaneous and time-averaged flowfields. The wake topology adapts in response to rotational speed variations, generating significant axial velocity gradients during the fastest maneuvers. The far wake retains features similar to those of the steady-state case before the start of the maneuver, as dynamic rpm changes occur over only a few propeller revolutions.

The influence of axial inflow velocity was also assessed. The fastest acceleration maneuver was repeated at different inflow velocities, revealing that deviations from steady-state conditions increase with higher V_∞. This behavior is attributed to the effects of low Reynolds number on the airfoil aerodynamic database. At low Reynolds numbers, the $c_L(\alpha)$ curves exhibit a pseudoquadratic shape, leading to larger slopes at lower angles of attack. Higher axial inflow velocities reduce the overall blade angle of attack, amplifying the load differences between steady-state and dynamic conditions.

Although the linear ramp considered in this study may not be optimal in terms of propeller performance, it provides a representative scenario for investigating the effects of rpm variation. More realistic maneuvers often follow exponential-like ramps, featuring sharp initial changes followed by slower stabilization. The main effects observed here, such as the induced velocity lag being proportional to

the maneuver intensity, are expected to extend to more complex maneuvers and different inflow conditions.

When the propeller operates in axial inflow, the wake evolves with organized flow structures along the axial direction, making instantaneous flowfields generally sufficient for a preliminary analysis of the main trends. However, more complex maneuvers or varying inflow conditions may require time-averaged fields to accurately capture the phenomenology. Such averaging is computationally expensive, as the full maneuver must be simulated rather than only a few revolutions as in steady-state cases. Midfidelity approaches, such as VPMs, provide an effective compromise, requiring moderate computational resources. Their ease of implementing dynamic maneuvers further enables the study of more complex and realistic rpm variations, enhancing the applicability of the results.

Appendix: Propeller's Thrust Undergoing an rpm Variation Maneuver

In this Appendix, the relationship between the induced velocity lag during dynamic rpm variation maneuvers and the resulting thrust variation is examined in detail. This lag primarily affects the angle of attack α and the relative velocity W experienced by the blade elements, thereby influencing the propeller loads. The thrust is shown to be particularly sensitive to changes in the angle of attack, which dominate over the effects of variations in the relative velocity, resulting in increased thrust during acceleration and decreased thrust during deceleration.

Focusing on an isolated blade element positioned at a distance r from the propeller hub, as illustrated in Fig. A1, the effect of the dynamic maneuver is assumed to act primarily in the plane of the blade element, perpendicular to the radial direction. For this element, the elementary contribution to the thrust $\mathrm{d}T$ is given by Eq. (A1), where $\mathrm{d}L$ and $\mathrm{d}D$ are the elementary lift and drag, respectively, and β is the blade pitch angle. Because the airfoil operates efficiently, the drag contribution can be neglected in the first approximation. Consequently, the elementary thrust can be expressed, as in Eq. (A2):

$$\mathrm{d}T = \mathrm{d}L\cos(\beta-\alpha) - \mathrm{d}D\sin(\beta-\alpha) \tag{A1}$$

$$\mathrm{d}T \approx \mathrm{d}L\cos(\beta-\alpha) = \frac{1}{2}\rho c c_L W^2(\beta-\alpha) \tag{A2}$$

The lift coefficient c_L can be approximated as a linear function of α for small angles of attack: $c_L \approx c_L'\alpha$, where c_L' is a positive constant. This approximation is most accurate at higher Re_c regimes, particularly for larger propellers than the one considered in this study. Nevertheless, it provides a general formulation to establish a qualitative trend of the thrust as a generic propeller accelerates or decelerates under axial inflow conditions.

As illustrated in Fig. A1, α and W^2 can be expressed in terms of the tangential and axial velocity components, as shown in Eq. (A3). The ratio between the axial velocity component $(V_\infty + v')$ and the tangential component $(\Omega r - u')$ is denoted as λ_v. Thus, the elementary thrust can be written as in Eq. (A4). The nondimensional quantity λ_v incorporates both induced velocity components, u' and v', which are

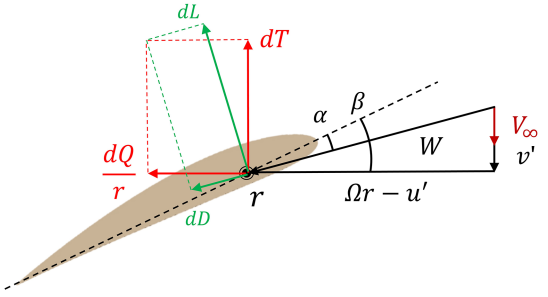

Fig. A1 Schematic representation of a blade element at a distance r from the propeller's hub.

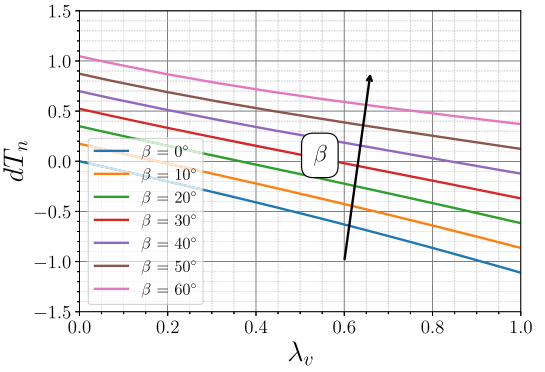

Fig. A2 Nondimensional elementary thrust $\mathrm{d}T_n$ as a function of λ_v for different values of β.

subject to a lag effect during dynamic rpm variation maneuvers. However, u' is typically an order of magnitude smaller than v' and Ωr. Therefore, in this context, λ_v is assumed to vary primarily with v'. All remaining quantities are considered positive and constant and can therefore be combined into a single factor, $k = 1/2\rho c c_L'(\Omega r - u')^2$, as expressed in Eq. (A5):

$$\mathrm{d}T = \frac{1}{2}\rho c c_L'\left(\beta - \operatorname{atan}\left(\frac{V_\infty + v'}{\Omega r - u'}\right)\right)((V_\infty + v')^2 + (\Omega r - u')^2)\cos\left(\operatorname{atan}\left(\frac{V_\infty + v'}{\Omega r - u'}\right)\right) \tag{A3}$$

$$\mathrm{d}T = \frac{1}{2}\rho c c_L'(\beta - \operatorname{atan}(\lambda_v))(\lambda_v^2 + 1)(\Omega r - u')^2\cos(\operatorname{atan}(\lambda_v)) \tag{A4}$$

$$\mathrm{d}T = k(\beta - \operatorname{atan}(\lambda_v))\cdot(\lambda_v^2 + 1)\cdot\cos(\operatorname{atan}(\lambda_v)) \tag{A5}$$

The nondimensional elementary thrust $\mathrm{d}T_n = \mathrm{d}T/k$ is shown as a function of λ_v in Fig. A2 for different values of β. In particular, the latter parameter is varied between 0 and 60 deg to account for a wide range of twist angles, considering both low-pitch and high-pitch propellers. Instead, λ_v is varied from 0 to 1 to cover an extensive range of possible operative conditions.

Regardless of the chosen β angle, $\mathrm{d}T_n$ is a monotonically decreasing function of λ_v, exhibiting an almost linear trend. Increasing β shifts the curves toward higher $\mathrm{d}T_n$ values without substantially altering their slopes. Although the term $(\lambda_v^2 + 1)$ associated with W^2 contributes to increasing thrust, the two terms related to α dominate within the analyzed range, resulting in the overall monotonically decreasing behavior. Small decreases in λ_v correspond to acceleration maneuvers, in which v' is lower than in the steady-state case. For any blade element and its associated β, this leads to an increased elementary thrust relative to the steady-state condition and consequently to a higher overall integral thrust. The opposite occurs during deceleration, in which λ_v increases, producing a lower thrust. A similar analysis could be performed for the elementary torque, but it is omitted here for conciseness. Additionally, a complete treatment would require accounting for both elementary drag and lift contributions, which would necessitate further assumptions on the free parameters.

Acknowledgments

This study is part of the project Piano Nazionale di Ripresa e Resilienza–Next Generation EU, which has received funding from MUR-DM352/2022. It was carried out within MOST: National Centre for Sustainable Mobility and received funding from the European Union Next Generation EU (Piano Nazionale di Ripresa e Resilienza–Missione 4 Componente 2, Investimento 1.4–D.D. 1033 17/06/2022, CN00000023). This paper reflects only the

authors' views and opinions, and neither the European Union nor the European Commission can be considered responsible for them. Alessandro Grava acknowledges ONERA for co-sponsoring the Ph.D. studentship. The authors acknowledge Johan Valentin for his support in the use of the VULCAINS code and for his valuable assistance in the interpretation of the results.

References

[1] Analytica, A., "Unmanned Aerial Vehicle (UAV) Market Valuation Skyrocketing to Reach US$ 119.71 Billion By 2032," Tech Rept., Astute Analytica, 2023, https://www.astuteanalytica.com/industry-report/unmanned-aerial-vehicle-market.

[2] Sauls, L. A., Paneque-Gálvez, J., Amador-Jiménez, M., Vargas-Ramírez, N., and Laumonier, Y., "Drones, Communities and Nature: Pitfalls and Possibilities for Conservation and Territorial Rights," *Global Social Challenges Journal*, Vol. 2, No. 1, 2023, pp. 24–46. https://doi.org/10.1332/AJHA9183

[3] Puri, V., Nayyar, A., and Raja, L., "Agriculture Drones: A Modern Breakthrough in Precision Agriculture," *Journal of Statistics and Management Systems*, Vol. 20, No. 4, 2017, pp. 507–518. https://doi.org/10.1080/09720510.2017.1395171

[4] Gargalakos, M., "The Role of Unmanned Aerial Vehicles in Military Communications: Application Scenarios, Current Trends, and Beyond," *Journal of Defense Modeling and Simulation*, Vol. 21, No. 3, 2024, pp. 313–321. https://doi.org/10.1177/15485129211031668

[5] Moradi, N., Wang, C., and Mafakheri, F., "Urban Air Mobility for Last-Mile Transportation: A Review," *Vehicles*, Vol. 6, No. 3, 2024, pp. 1383–1414. https://doi.org/10.3390/vehicles6030066

[6] Hein, B. R., and Chopra, I., "Hover Performance of a Micro Air Vehicle: Rotors at Low Reynolds Number," *Journal of the American Helicopter Society*, Vol. 52, No. 3, 2007, pp. 254–262. https://doi.org/10.4050/JAHS.52.254

[7] Ramasamy, M., Johnson, B., and Leishman, J. G., "Understanding the Aerodynamic Efficiency of a Hovering Micro-Rotor," *Journal of the American Helicopter Society*, Vol. 53, No. 4, 2008, pp. 412–428. https://doi.org/10.4050/JAHS.53.412

[8] Milluzzo, J., and Leishman, J. G., "Fluid Dynamics of the Helicoidal Wake Sheets Trailed From a Hovering Rotor," *Journal of the American Helicopter Society*, Vol. 61, No. 1, 2016, pp. 1–17. https://doi.org/10.4050/JAHS.61.012002

[9] Carreño Ruiz, M., Scanavino, M., D'Ambrosio, D., Guglieri, G., and Vilardi, A., "Experimental and Numerical Analysis of Hovering Multicopter Performance in Low-Reynolds Number Conditions," *Aerospace Science and Technology*, Vol. 128, 2022, Paper 107777. https://doi.org/10.1016/j.ast.2022.107777

[10] Grava, A., Serpieri, J., Iuso, G., Bernardos, L., and Cafiero, G., "Experimental Investigation of a Small Drone Propeller Aerodynamics in Forward Flight," *AIAA Journal*, Vol. 63, No. 5, 2025, pp. 1855–1866. https://doi.org/10.2514/1.J064664

[11] Grava, A., Picillo, M., Serpieri, J., Iuso, G., Bernardos, L., and Cafiero, G., "Aerodynamic Investigation of a Drone Propeller in Cross-Flow," *AIAA SCITECH 2024 Forum*, AIAA Paper 2024-0244, 2024. https://doi.org/10.2514/6.2024-0244

[12] Yang, Y., Liu, Y., Li, Y., Arcondoulis, E., and Wang, Y., "Aerodynamic and Aeroacoustic Performance of an Isolated Multicopter Rotor during Forward Flight," *AIAA Journal*, Vol. 58, No. 3, 2020, pp. 1171–1181. https://doi.org/10.2514/1.J058459

[13] Cerny, M., and Breitsamter, C., "Investigation of Small-Scale Propellers Under Non-Axial Inflow Conditions," *Aerospace Science and Technology*, Vol. 106, Nov. 2020, Paper 106048. https://doi.org/10.1016/j.ast.2020.106048

[14] Jamaluddin, N. S., Celik, A., Baskaran, K., Rezgui, D., and Azarpeyvand, M., "Aerodynamic Noise Analysis of Tilting Rotor in Edgewise Flow Conditions," *Journal of Sound and Vibration*, Vol. 582, July 2024, Paper 118423. https://doi.org/10.1016/j.jsv.2024.118423

[15] Grande, E., Romani, G., Ragni, D., Avallone, F., and Casalino, D., "Aeroacoustic Investigation of a Propeller Operating at Low Reynolds Numbers," *AIAA Journal*, Vol. 60, No. 2, 2022, pp. 860–871. https://doi.org/10.2514/1.J060611

[16] Grande, E., Ragni, D., Avallone, F., and Casalino, D., "Laminar Separation Bubble Noise on a Propeller Operating at Low Reynolds Numbers," *AIAA Journal*, Vol. 60, No. 9, 2022, pp. 5324–5335. https://doi.org/10.2514/1.J061691

[17] Newman, S., "Principles of Helicopter Aerodynamics–Second edition JG Leishmann Cambridge University Press, The Edinburgh Building, Shaftesbury Road, Cambridge, CB2 2RU, UK. 2006. 826pp. Illustrated.£ 65. ISBN 0-521-85860-7," *Aeronautical Journal*, Vol. 111, No. 1126, 2007, pp. 825–826.

[18] Brotherhood, P., and Stewart, W., "An Experimental Investigation of the Flow Through a Helicopter Rotor in Forward Flight," 1949.

[19] Cheeseman, I., and Bennett, W., "The Effect of the Ground on a Helicopter Rotor in Forward Flight," 1955.

[20] Rajagopalan, R. G., and Mathur, S. R., "Three Dimensional Analysis of a Rotor in Forward Flight," *Journal of the American Helicopter Society*, Vol. 38, No. 3, 1993, pp. 14–25. https://doi.org/10.4050/JAHS.38.14

[21] Pérez Gordillo, A. M., Escobar, J. A., and Lopez Mejia, O. D., "Influence of the Reynolds Number on the Aerodynamic Performance of a Small Rotor," *Aerospace*, Vol. 10, No. 2, 2023, Paper 130. https://doi.org/10.3390/aerospace10020130

[22] Winslow, J., Otsuka, H., Govindarajan, B., and Chopra, I., "Basic Understanding of Airfoil Characteristics at Low Reynolds Numbers (10^4–10^5)," *Journal of Aircraft*, Vol. 55, No. 3, 2018, pp. 1050–1061. https://doi.org/10.2514/1.C034415

[23] Wang, S., Zhou, Y., Alam, M. M., and Yang, H., "Turbulent Intensity and Reynolds Number Effects on an Airfoil at Low Reynolds Numbers," *Physics of Fluids*, Vol. 26, No. 11, 2014. https://doi.org/10.1063/1.4901969

[24] Mueller, T. J., and DeLaurier, J. D., "Aerodynamics of Small Vehicles," *Annual Review of Fluid Mechanics*, Vol. 35, No. 1, 2003, pp. 89–111. https://doi.org/10.1146/annurev.fluid.35.101101.161102

[25] Möhren, F., Bergmann, O., Braun, C., and Janser, F., "Prediction and Comparison of Dynamic Loads of Propellers," *AIAA SciTech 2022 Forum*, AIAA Paper 2022-2267, 2022. https://doi.org/10.2514/6.2022-2267

[26] Bergmann, O., Möhren, F., Braun, C., and Janser, F., "Propeller Noise Prediction for Transient eVTOL Missions," *AIAA SCITECH 2024 Forum*, AIAA Paper 2024-2636, 2024. https://doi.org/10.2514/6.2024-2636

[27] Pavel, M. D., "Understanding the Control Characteristics of Electric Vertical Take-Off and Landing (eVTOL) Aircraft for Urban Air Mobility," *Aerospace Science and Technology*, Vol. 125, June 2022, Paper 107143. https://doi.org/10.1016/j.ast.2021.107143

[28] Zosimovych, N., "Flight Transient Estimation of VTOL Aircraft with Propellers," *Advances in Aerospace Science and Technology*, Vol. 7, No. 1, 2022, pp. 85–95. https://doi.org/10.4236/aast.2022.71005

[29] Podsędkowski, M., Konopiński, R., Obidowski, D., and Koter, K., "Variable Pitch Propeller for UAV-Experimental Tests," *Energies*, Vol. 13, No. 20, 2020, Paper 5264. https://doi.org/10.3390/en13205264

[30] Valentin, J., and Bernardos, L., "Validation of a New Solver Based on the Vortex Particle Method for Wings, Propellers and Rotors," *ERF-European Rotorcraft Forum 2023*, 2023.

[31] Valentin, J., Bernardos, L. F., Pinon, G., and Rivoalen, E., "Hybrid Eulerian–Lagrangian Method for Complex 3D Viscous Flows," *AIAA AVIATION FORUM and ASCEND 2024*, AIAA Paper 2024-3865, 2024. https://doi.org/10.2514/6.2024-3865

[32] Singh, P., and Friedmann, P. P., "Application of Vortex Methods to Coaxial Rotor Wake and Load Calculations in Hover," *Journal of Aircraft*, Vol. 55, No. 1, 2018, pp. 373–381. https://doi.org/10.2514/1.C034520

[33] Alvarez, E. J., and Ning, A., "Modeling Multirotor Aerodynamic Interactions Through the Vortex Particle Method," *AIAA Aviation 2019 Forum*, AIAA Paper 2019-2827, 2019. https://doi.org/10.2514/6.2019-2827

[34] Lee, H., and Lee, D.-J., "Numerical Investigation of the Aerodynamics and Wake Structures of Horizontal Axis Wind Turbines by Using Nonlinear Vortex Lattice Method," *Renewable Energy*, Vol. 132, March 2019, pp. 1121–1133. https://doi.org/10.1016/j.renene.2018.08.087

[35] Stock, M., Gharakhani, A., and Stone, C., "Modeling Rotor Wakes with a Hybrid OVERFLOW-Vortex Method on a GPU Cluster," *28th AIAA Applied Aerodynamics Conference*, AIAA Paper 2010-4553, 2010. https://doi.org/10.2514/6.2010-4553

[36] Chatelain, P., Duponcheel, M., Caprace, D.-G., Marichal, Y., and Winckelmans, G., "Vortex Particle-Mesh Simulations of Vertical Axis Wind Turbine Flows: From the Airfoil Performance to the Very Far

Wake," *Wind Energy Science*, Vol. 2, No. 1, 2017, pp. 317–328. https://doi.org/10.5194/wes-2-317-2017

[37] Tan, J., Sun, Y., and Barakos, G., "Unsteady Loads for Coaxial Rotors in Forward Flight Computed Using a Vortex Particle Method," *Aeronautical Journal*, Vol. 122, No. 1251, 2018, pp. 693–714. https://doi.org/10.1017/aer.2018.8

[38] Grava, A., Serpieri, J., Bernardos, L., and Cafiero, G., "Multi-Fidelity Analysis of a Small-Scale Propeller Using VPM Against URANS and Experimental Data," *AIAA AVIATION 2025 Forum*, AIAA Paper 2025-3163, 2025. https://doi.org/10.2514/6.2025-3163

[39] Valentin, J., "Multi-Fidelity Vortex Particles Coupling with Lifting Line and Eulerian Methods for 3D Viscous Aeronautical Simulations," Ph.D. Thesis, INSA Rouen Normandy, Saint-Étienne-du-Rouvray, France, 2024.

[40] Mansfield, J. R., Knio, O. M., and Meneveau, C., "Dynamic LES of Colliding Vortex Rings Using a 3D Vortex Method," *Journal of Computational Physics*, Vol. 152, No. 1, 1999, pp. 305–345. https://doi.org/10.1006/jcph.1999.6258

[41] Alvarez, E. J., and Ning, A., "Reviving the Vortex Particle Method: A Stable Formulation for Meshless Large Eddy Simulation," arXiv preprint arXiv:2206.03658, 2022. https://doi.org/10.48550/arXiv.2206.03658

[42] Mansfield, J. R., Knio, O. M., and Meneveau, C., "A Dynamic Les Scheme for the Vorticity Transport Equation: Formulation Anda Priori tests," *Journal of Computational Physics*, Vol. 145, No. 2, 1998, pp. 693–730. https://doi.org/10.1006/jcph.1998.6051

[43] Wang, T., Yokota, R., and Barba, L. A., "ExaFMM: A High-Performance Fast Multipole Method Library with C++ and Python Interfaces," *Journal of Open Source Software*, Vol. 6, No. 61, 2021, Paper 3145. https://doi.org/10.21105/joss.03145

[44] Mycek, P., Pinon, G., Germain, G., and Rivoalen, É., "A Self-Regularising DVM–PSE Method for the Modelling of Diffusion in Particle Methods," *Comptes Rendus Mécanique*, Vol. 341, Nos. 9–10, 2013, pp. 709–714. https://doi.org/10.1016/j.crme.2013.08.002

[45] Mycek, P., Pinon, G., Germain, G., and Rivoalen, E., "Formulation and Analysis of a Diffusion-Velocity Particle Model for Transport-Dispersion Equations," *Computational and Applied Mathematics*, Vol. 35, No. 2, 2016, pp. 447–473. https://doi.org/10.1007/s40314-014-0200-5

[46] Mas-Gallic, S., "The Diffusion Velocity Method: A Deterministic Way of Moving the Nodes for Solving Diffusion Equations," *Transport Theory and Statistical Physics*, Vol. 31, Nos. 4–6, 2002, pp. 595–605. https://doi.org/10.1081/TT-120015516

[47] Yokota, R., Barba, L. A., Narumi, T., and Yasuoka, K., "Petascale Turbulence Simulation Using a Highly Parallel Fast Multipole Method on GPUs," *Computer Physics Communications*, Vol. 184, No. 3, 2013, pp. 445–455. https://doi.org/10.1016/j.cpc.2012.09.011

[48] Tollmien, W., Schlichting, H., Görtler, H., and Riegels, F., "Bericht über Untersuchungen Zur Ausgebildeten Turbulenz," *Ludwig Prandtl Gesammelte Abhandlungen: Zur Angewandten Mechanik*, Hydro-und Aerodynamik, 1961, pp. 714–718.

[49] Kwak, D., Reynolds, W. C., and Ferziger, J. H., "Three-Dimensional Time Dependent Computation of Turbulent Flow," Tech. Rept., 1975.

[50] Vreman, A., "An Eddy-Viscosity Subgrid-Scale Model for Turbulent Shear Flow: Algebraic Theory and Applications," *Physics of Fluids*, Vol. 16, No. 10, 2004, pp. 3670–3681. https://doi.org/10.1063/1.1785131

[51] Pedrizzetti, G., "Insight into Singular Vortex Flows," *Fluid Dynamics Research*, Vol. 10, No. 2, 1992, pp. 101–115. https://doi.org/10.1016/0169-5983(92)90011-K

[52] Backaert, S., Chatelain, P., and Winckelmans, G., "Vortex Particle-Mesh with Immersed Lifting Lines for Aerospace and Wind Engineering," *Procedia IUTAM*, Vol. 18, 2015, pp. 1–7. https://doi.org/10.1016/j.piutam.2015.11.001, iUTAM Symposium on Particle Methods in Fluid Dynamics.

[53] Caprace, D.-G., Winckelmans, G., and Chatelain, P., "An Immersed Lifting and Dragging Line Model for the Vortex Particle-Mesh Method," *Theoretical and Computational Fluid Dynamics*, Vol. 34, No. 1, 2020, pp. 21–48. https://doi.org/10.1007/s00162-019-00510-1

[54] Grava, A., "Aerodynamics of a Small-Scale Drone Propeller in Challenging Operative Conditions," Ph.D. Thesis, Politecnico di Torino, Turin, Italy, 2026.

[55] Critzos, C. C., Heyson, H. H., and Boswinkle, R. W., Jr., "Aerodynamic Characteristics of NACA, 0012 Airfoil Section at Angles of Attack from 0 deg to 180 deg," NASA TN 3361, 1955.

[56] Jeong, J., and Hussain, F., "On the Identification of a Vortex," *Journal of Fluid Mechanics*, Vol. 285, 1995, pp. 69–94. https://doi.org/10.1017/S0022112095000462

[57] Hunt, J., Wray, A., and Moin, P., "Eddies, Streams, and Convergence Zones in Turbulent Flows," *Studying Turbulence Using Numerical Simulation Databases*, Vol. 1, Dec. 1988, pp. 193–208.

[58] Cafiero, G., Castrillo, G., Greco, C., and Astarita, T., "On the Effects of Square-Fractal Turbulators on the Flow Field Generated by a Synthetic Jet Actuator," *Experimental Thermal and Fluid Science*, Vol. 102, April 2019, pp. 302–315. https://doi.org/10.1016/j.expthermflusci.2018.12.005

[59] Zaccara, M., Paolillo, G., Cafiero, G., Astarita, T., Iuso, G., Cardone, G., and Greco, C. S., "Near Field Evolution of Wingtip Vortices Under Synthetic-Jet Based Control," *Aerospace Science and Technology*, Vol. 148, May 2024, Paper 109068. https://doi.org/10.1016/j.ast.2024.109068

[60] Xia, T., Dong, H., Yang, L., Liu, S., and Jin, Z., "Investigation on Flow Structure and Aerodynamic Characteristics over an Airfoil at Low Reynolds Number—A Review," *AIP Advances*, Vol. 11, No. 5, 2021, Paper 050701. https://doi.org/10.1063/5.0044717

K. A. Morgansen
Associate Editor